

Latest Edition

Welcome to the August 2015 edition of TCAD News. This edition covers the K-2015.06 release of Sentaurus. Its focus is on supporting the development of sub-10nm logic technologies, new memory technologies and the broadening of applications in power devices and opto-electronics. Among the many new features and enhancements you will find in Sentaurus Process a new model for epi growth using the lattice KMC method, enhancements to modeling solid-phase epitaxial regrowth, and a very useful utility for building analytical implant tables. Sentaurus Interconnect has been significantly enhanced with the addition of mixed element meshes, which provide greater flexibility in the thermo-mechanical modeling of large structures. In Sentaurus Device, a comprehensive set of models has been added to simulate quantization and device transport effects in III-V CMOS devices. Sentaurus Device Monte Carlo has been enhanced with screened ionized impurity scattering and the subband and low-field mobility calculation can now solve III-V bandstructure problems and account for surface roughness scattering. In this edition we also report on the new capabilities introduced in March 2015 for modeling spin-transfer torque RAM (STT-RAM) in Sentaurus Device. Sentaurus Device EMW, an important component of image sensor simulation, has been enhanced in the areas of far-field computation and real-time convergence monitoring.

Overall, the new release of TCAD Sentaurus has an impressive list of enhancements that extends the modeling coverage for both More Moore and More than Moore devices. I trust that you will find the new enhancements in the K-2015.06 release of TCAD Sentaurus useful for your simulation tasks. As always I welcome your feedback.

With warm regards,

Terry Ma
Vice President of Engineering, TCAD

Contact TCAD

For further information and inquiries:
tcad_team@synopsys.com

TCAD news

Sentaurus Process

The simulation of front-end wafer processing has considerable economic and technological value. The success and pervasive influence of the microelectronics industry is largely built upon the techniques for processing silicon and related materials into progressively faster and more functional solid-state circuits. With successive generations of silicon technologies, the process complexity and development cost has risen considerably. Moreover, as transistor dimensions shrink it has become increasingly difficult and expensive to characterize the physical properties of the materials (doping, defect levels, shapes, mechanical stress, etc) comprising the transistor structure. As the leading process simulator in the market, Sentaurus Process continues to evolve to reflect the needs of the latest technologies. This section describes important new features and enhancements in Sentaurus Process, targeting the latest applications and improving usability.

Silicon Nitridation

Nitridation of silicon injects vacancies into the silicon regions, contributing to a reduction of interstitial clusters and to an enhancement

of vacancy-mediated dopant diffusion.

The need to properly account for the interstitial-vacancy balance has motivated the introduction of a more rigorous model in Sentaurus Process to simulate nitridation and the related vacancy injection. The nitride is grown by consuming silicon on an exposed silicon surface in a NH₃ gas environment. The vacancy injection is modeled in a similar way as interstitial injection during oxidation. The command to activate the simulation of silicon nitridation is:

```
diffuse temp= <temperature>
time=<time> NH3
```

The simulation of nitride growth during nitridation is based on the Deal-Grove model. The default parameter values are calibrated against published data [1]. Figure 1 compares simulated and measured data. Since the orientation dependence of nitridation is negligible, the model parameters are applied to all orientations. Due to lack of experimental data, neither pressure nor Fermi-level dependences are taken into account in the default parameter set.

In This Edition

Sentaurus Process.....	1	Sentaurus Device	
Sentaurus Process Kinetic		Optoelectronics.....	11
Monte Carlo	3	Usability Improvements.....	12
Sentaurus Interconnect.....	4	Sentaurus Visual	14
Sentaurus Device	5	Sentaurus Workbench	15
Simulation of Spin-Transfer			
Torque Devices Using			
Sentaurus Device Spintronics	9		

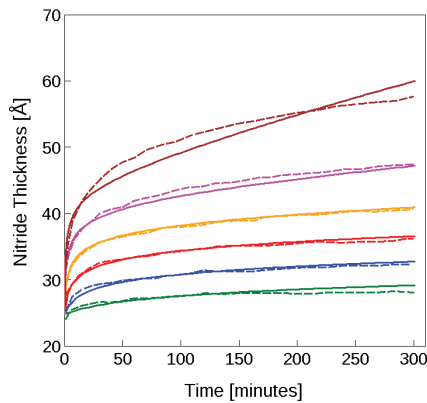


Figure 1: Comparison of simulated and measured nitride layer thicknesses as a function of growth time. The solid lines show simulated and the dashed lines experimental data. The ambient temperatures are 950 (green), 1000 (blue), 1050 (red), 1100 (orange), 1050 (magenta), and 1200°C (brown)

Improvement in Automatic Generation of Implantation Tables

`ImplantTableMaker` is a useful utility which can be conveniently used to create analytic implantation tables from Monte Carlo (MC) implantations during the simulation run itself. In this release, several important improvements have been made to the utility in order to increase its robustness and ease-of-use:

- ▶ **Automatic fitting quality check and re-run of MC implantation simulations (if necessary) by using root mean square (RMS) error:** RMS error is an important gauge for the fitting accuracy in implant moment extraction. Generally, if the RMS error is less than 1, the fitting is visually acceptable. On the other hand, if the RMS error is greater than 10, the fitting is poor. After each extraction, `ImplantTableMaker` checks the returned value of the RMS error. If it is greater than the specified value, it will automatically rerun the MC implant simulations with twice the particle number, and then re-initiate the extraction.
- ▶ **Support for both interactive and batch modes:** When `ImplantTableMaker` is started for the first time, it will enter

interactive mode and will request from the user the implant conditions and control parameters which are necessary to run the MC implant simulations and to create the table. These user inputs are then recorded in a text file, which can then be edited and re-read by `ImplantTableMaker` in a subsequent batch mode run.

This eliminates the need to enter the same information several times when `ImplantTableMaker` is re-launched.

- ▶ **Extract more consistent moments by imposing certain constraints during the extraction:** After a MC simulation, `ImplantTableMaker` analyzes the profile and calculates the upper and lower bounds of the projected range (R_p) which are then used as constraint for the extraction. In addition, R_p for the second Pearson distribution is now guaranteed to be greater than R_p for the first Pearson distribution. These constraints do not necessarily improve the fits for a given implant condition, but will usually generate more consistent neighboring table entries.
- ▶ **Print warning messages if certain moment extraction does not converge:** If the extraction does not converge after the maximum number of iterations, a warning message is printed, and the data file is kept (not removed) for user inspection or manually extraction.

The capability of this new utility is shown in the following example. The implant table was created by specifying Arsenic implantation energies of 20, 30, and 40 keV, doses of 10^{13} , 10^{14} , and 10^{15} cm^{-2} , and tilt and rotation angle of 0° . All other control parameters use default values. Then by using the newly created implant table analytic implants are performed with the same implant conditions (shown as "Fit" in Figure 2).

Two additional analytic implants are shown with dose (top panel) and energy (bottom panel) parameters in between the values used for the table generation (labeled as "Interpolation"). It can be seen that due to the constraints, the fits to MC implant results are not perfect; however, the constraints ensure

that the interpolated curves exhibit a very reasonable behavior.

Even with these significant improvements, the complexity of implant table extraction still precludes automated implant table creation, and is expected to require some level of human intervention for the foreseeable future.

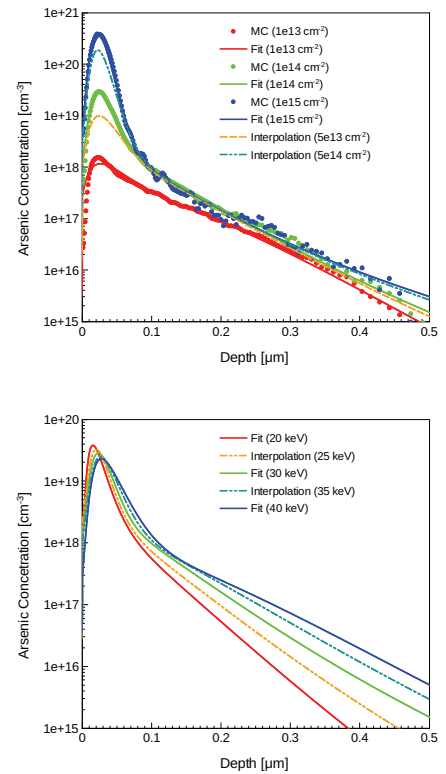


Figure 2: Implant profiles by using the implant table created by `ImplantTableMaker`. Dose dependence (top). Energy dependence (bottom). The curves labeled "Fit" compare analytic implant results obtained with these implant tables to the original MC data using the same implant conditions. The curves labeled "Interpolation" show results for implant conditions with either doses or energies in-between the values used for creating the tables.

Defining a Doping Profile within Polyhedron

Simulation of modern 3D devices often involves doping profiles defined analytically and through physical simulation of the doping process. The need for analytic profiles emerges from lack of calibrated physical models that cover the wide range

of materials in device structures, which are often subjected to strain engineering. Previously, the only way to generate cuboid-based analytic profiles with error function roll-off was to use the `select` command. This required the construction of an equation consisting of a superposition of a large number of error functions, a somewhat cumbersome procedure.

With Sentaurus Process K-2015.06 users now place a uniform doping within a user-defined polyhedron without inserting any new material and without triggering a remeshing step. This new capability is activated with the `polyhedron` option of the `profile` command:

```
profile name=<c>
concentration=<n>
polyhedron=<c> x.sigma=<n>
y.sigma=<n> z.sigma=<n>
```

where `polyhedron` specifies a name of the polyhedron as defined in a previous `polyhedron` command. When the polyhedron is defined through the `brick` option of the `polyhedron` command, the user can specify different values of profile roll-off parameters `sigma` (`x.sigma`, `y.sigma`, and `z.sigma`) for each of the three principal axes. Otherwise, only a single roll-off function (`x.sigma`) is allowed. The roll off is computed by using the nearest distance to the polyhedron.

Sentaurus Process Kinetic Monte Carlo

Kinetic Monte Carlo (KMC) is an alternative method to continuum process simulation which is becoming increasingly important in state-of-the-art process modeling. As more materials are being explored and thermal budgets are reduced, traditional PDE-based algorithms become more and more complex and computationally expensive, to the point where Monte Carlo-based algorithms become practical alternatives. Moreover, continuum methods are not conducive to the investigation of atomistic statistical fluctuations of dopants and defects in nanometer scale devices, whereas KMC

methods offer a natural way to track discrete dopant and defect distributions. Therefore, KMC and its closely related method Lattice Kinetic Monte Carlo (LKMC) are expected to become important components of TCAD simulation flows in advanced processes, particularly in FinFET and nanowire FET applications.

The KMC method considers only defects and impurities, and ignores the host lattice as it follows only the dynamic evolution of dopants, point defects and extended defects. The LKMC method, on the other hand, preserves the representation of the host lattice and uses it as a template for modeling epitaxial growth and other process techniques for which the crystalline state is importance. Both methods complement each other and are the subject of considerable development within the Sentaurus Process platform. This section describes key new features in KMC and LKMC.

Solid Phase Epitaxial Regrowth (SPER)

A new stress correction model to lattice kinetic Monte Carlo (LKMC) SPER based on Sklenard et al. [2] has been introduced in Sentaurus Process KMC K-2015.06. This model depends on the number of nearest and next-nearest crystalline neighbors, and thus displays bimodal growth in the [100] direction. The prefactor associated with the [100] direction is split into two contributions depending on whether the sum of nearest and next nearest crystalline neighbors is greater than 8 (highly crystalline) or not. The model computes a correction to the regrowth energy barrier based on the stress.

Reduced Minimum Cell Size

The minimum cell size available for creating KMC internal meshes has been reduced from 0.8nm to 0.4nm. When the minimum cell size is reduced to below 0.8nm, the double hop and long hop models are switched off in order to preserve accuracy. This feature is important for preserving the integrity and fidelity of thin layers.

The impact of reducing the minimum cell size is illustrated in Figure 3. The left panel shows the continuum geometry. A thin layer (0.6nm) of interfacial oxide was deposited onto the silicon fin, followed by a nitride deposition on top of the interfacial oxide, leading to a curved top. The middle and right panels are internal KMC representations of the same geometry. For clarity, only interfacial oxide and Nitride/Gas boundaries are shown in the middle and right panels. It can be seen that when translating the continuum geometry to KMC for the case with `YMinCell` set to 0.8nm (middle panel), more than two thirds of the interfacial oxide is lost, leaving only one vertical slice. Also the pixilated "Manhattan" steps on top of Nitride are a very rough approximation of the original curved surface. With `YMinCell` reduced to 0.4nm (right panel), the integrity of interfacial oxide is preserved and the representation of the nitride surface is also much improved.

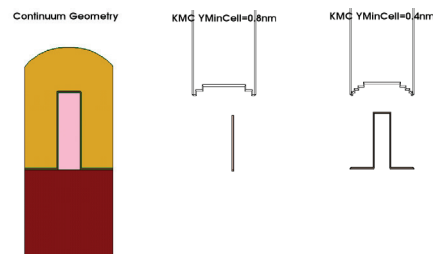


Figure 3: Continuum structure (left). Pixilated KMC version of the same structure using a 0.8nm minimum cell size (middle). Same structure, but using a 0.4nm minimum cell size (right). For clarity, only interfacial oxide and Nitride/Gas boundary are shown in the middle and right panels

In addition, the spacing argument of the `line` command has been improved with respect to the creation of KMC meshes, producing now tensor-mesh spacing and line placement in exact agreement with the user specification.

New Approach to KMC Material Handling

In previous releases, parameters from all known KMC materials were read in regardless of need. In addition, when users defined new Sentaurus Process materials,

they were not automatically available to KMC unless they were specifically requested via the `KMC Materials` parameter.

In this release, KMC and LKMC parameters are automatically read in only for those materials present in the structure. This reduces KMC simulation times, especially for short runs.

This feature is activated through the specification of new materials with the `mater` command and with the `new.like` argument in the same way as in continuum simulations. After a new material is defined in Sentaurus Process, it is automatically available for KMC and LKMC simulations. For more information, please refer to section “Supported Material Models” of Chapter 5 of the Sentaurus Process User Guide.

Parameter Inheritance

Creating new materials which inherit material parameters from an existing material is a convenient way to enable special handling of regions and prevent merging of these regions with other regions of the same material. Inheriting parameters is normally done by specifying `mater add name= <my new material> new.like = <existing material>`. This capability is now also fully supported in KMC without requiring any additional specification (such as including the parameter `KMC Materials`).

New LKMC Epitaxy Model

A new model for simulating selective epitaxy deposition (SEG), named the “Coordinations” model has been developed. This model is purely atomistic, allowing for the specification of process input parameters such as epitaxy gas flows instead of results-oriented parameters such as layer thickness and doping concentrations. In this model the epitaxial growth rates depend on doping concentration, crystal orientation and mole fraction of the already grown layer. The doping concentration and mole fraction in the *growing* layer in turn depend on temperature, as well crystal orientation and mole fraction of the already grown layer

Figure 4 shows as an example an epitaxially grown SiGe source/drain region a FinFET.

The new LKMC epitaxial growth model requires extensive calibration before it can be used in a predictive fashion. **General calibration of this model is ongoing and sets of calibrated parameters will be made available later this year. Until then this model should be regarded as a prototype.**

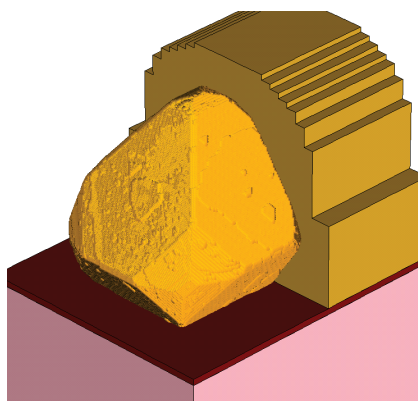


Figure 4: Epitaxial grown SiGe region (shown in yellow) created using the new epitaxial growth model named `Coordinations`.

Layout and Mask-driven Simulations in Sentaurus Process and Sentaurus Interconnect

For 2D TCAD simulations, it can be useful to work with composite simulation domains, for example, when the different contacts of a device cannot be connected by a single straight line in the layout. In such cases, the various 2D cuts in the layout are joined to form a composite 2D simulation domain.

Support for such composite simulation domains has been available in IC Workbench EV Plus. In the K-2015.06 release, composite simulation domains are also supported when using the GDSII reader in Sentaurus Process and Sentaurus Interconnect.

Further, when using mask-driven contact assignments users are no longer required to provide a height coordinate. This information is determined automatically by analyzing the layer stack.

Before creating a mask from a layer, users can first apply several different transformations, such as a shift, or a stretch. Reflection of a layer around an axis is also possible.

Since it is inefficient to store masks with many vertices in the TDR file together with the device structure—such as for example masks with shapes computed from lithography simulations—users are now able to prevent Sentaurus Process and Sentaurus Interconnect from storing such masks in the TDR file. It is also possible to limit the storing to masks with a small number of vertices. The customization can be done globally or on a per mask basis.

Sentaurus Interconnect Mixed Meshes for Mechanical Simulations

Finding numerical solutions to stress equilibrium equations for a complex problem requires discretization of the entire continuum domain, using a mesh consisting of many (small) elements and approximation of deformations within each element, using shape functions.

Among the four types of 3D elements (tetrahedral, brick, prism, and pyramid), the brick element is superior in representing elemental deformation while the tetrahedral element offers superior flexibility in meshing complex geometries. Therefore, the optimal discretization for a mechanics simulation should utilize a mixed mesh, combining brick elements for accuracy and efficiency, tetrahedral elements for boundary fidelity, and prism and pyramid elements to enable smooth transitions between brick and tetrahedral elements with the requisite accuracy. Compared to a mesh with all tetrahedral elements, a mixed mesh with four types of elements provides improved solution accuracy, higher mesh quality, and reduced element count. Brick elements are especially useful in bending simulations since they alleviate the so-called shear locking phenomenon. Brick elements are,



therefore, an important component of mixed meshes to improve overall mesh quality, simulation runtime and accuracy. Similar observations can be made for the two types of 2D elements (triangular and rectangular elements).

Mixed meshes are available in this release to perform first-order mechanics simulations with support for all available material models: isotropic elastic, anisotropic elastic, viscoelastic, plastic, viscoplastic, creep and swelling. In addition, sub-modeling can also be carried out with mixed meshes. One of the key applications envisioned for mixed meshes is fracture mechanics—crack analysis and cohesive zone modeling (CZM), including the calculation of J and C_I integrals.

Figure 5 shows the usage of a brick mesh in a CZM analysis of two blocks with an interface crack subjected to displacement loading.

Although the brick mesh provides similar displacement results as a tetrahedral mesh, it uses approximately 6 times fewer elements. Moreover, as depicted in the x-direction normal stress distributions shown in Figure 6, the brick mesh has a more uniform stress distribution compared to the tetrahedral mesh.

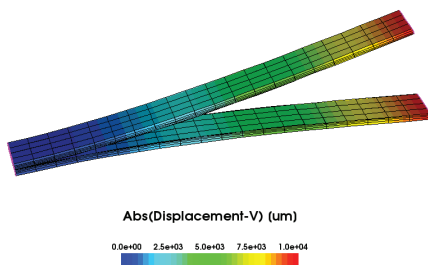


Figure 5: CZM analysis performed using a brick mesh, on two blocks with interface crack, subject to displacement loading.

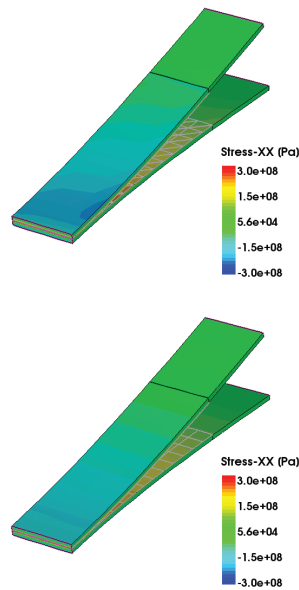


Figure 6: Comparison of stress distribution for tetrahedral (top) and brick meshes (bottom).

The implementation of the mixed mesh elements has been carried out through the introduction of a new finite element library, which provides the flexibility to integrate over different element types. Since these elements have different numbers of integration points (4 integration points for rectangular elements, 5 for pyramids, 8 for bricks, 1 for tetrahedrals and triangles), the concept of element centered integration/data points is no longer valid. In the new library, volume data, such as stress and strain, are now defined over *gauss points* instead of *elements*. While element fields recognized by the “_EL” suffix are still available for visualization, these are calculated from gauss point fields recognized by the “_GP” suffix during post-processing.

In addition to mechanics simulations, certain process and geometry options are also supported in mixed meshes. These include transformation operations (rotate, flip and reflect), where the data fields defined on the nodes and gauss points of bilinear quadrilateral elements, tri-linear pyramids, prism and hexahedron elements are handled accordingly, and process steps (etch, deposit and strip).

If the starting structure has mixed mesh elements, all subsequent etching and deposition operations are also performed in mixed mesh mode. Figure 7 shows a sequence of such process steps applied to a structure meshed initially with only brick elements (Figure 7 top-left). First a thin layer of oxide is deposited followed with a thick layer of deposited polysilicon. The structure is patterned with a mask and Polysilicon is etched anisotropically (Figure 7 top-right). Up to this point all the elements in the structure are kept as brick elements. When an isotropic nitride layer is deposited on top of the structure, the conformal curved faces create the need to insert transitional prism and pyramid elements (Figure 7 bottom-left). Then the nitride and oxide layers are etched anisotropically to form the final structure (Figure 7 bottom-right). Stress relaxation or other mechanical simulations can be carried as usual during these process steps.

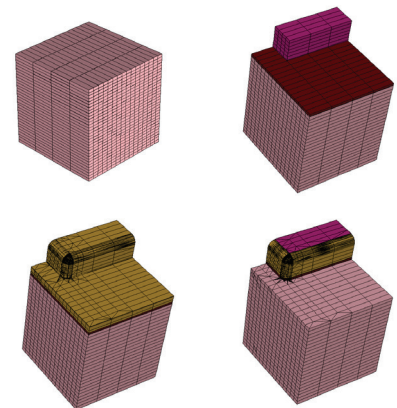


Figure 7: Sequence of etch, deposit, and strip process steps applied to a structure meshed initially exclusively with brick elements.

Sentaurus Device

Anisotropic Scharfetter-Gummel Discretization Scheme for Stress

Simulation of devices with anisotropic materials requires special discretization schemes to ensure accurate results and stable simulations. In Sentaurus Device J-2014.09, a novel discretization scheme was introduced which provided better



accuracy for certain meshes. This first release supported anisotropic dielectric permittivity, thermal conductivity, and mobility. In Sentaurus Device K-2015.06, this discretization scheme now also supports stress-induced effects via the Piezo models.

This new **StressSG** discretization scheme addresses limitations in the two previous discretization schemes (**AverageAniso** and **TensorGridAniso**) under certain mesh conditions. In both previous schemes, the accuracy of the solution depends on the relative orientation of the eigen-directions of mobility tensor and the mesh edge directions. In particular the **AverageAniso** scheme uses a local linear transformation, which transforms an anisotropic problem to an isotropic case. This method provides good accuracy only if the transformed mesh is also Delaunay mesh (which is sometimes not the case). The **TensorGridAniso** discretization scheme gives best results when the mesh is a tensor grid and the mobility tensor is diagonal. The new **StressSG** discretization scheme, however, has no dependence on mesh orientation and allows for a full mobility tensor. Figure 8 shows the improvement in accuracy by switching from the **TensorGridAniso** to **StressSG** scheme.

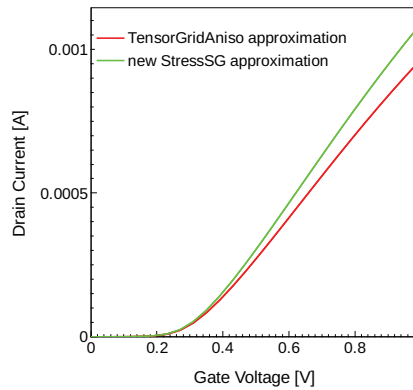


Figure 8: YY component of the mobility tensor for a MOSFET (top). Difference in IdVg results by switching from the TensorGridAniso to the more accurate stressSG discretization scheme.

Piezoelectric Polarization from Strain

Piezoelectric polarization plays a critical role in the device performance of III-Nitride semiconductors. Starting with the K-2015.06 release, Sentaurus Device offers a new model to compute the piezoelectric polarization vector P as a function of the strain tensor ϵ :

$$\begin{bmatrix} P_x \\ P_y \\ P_z \end{bmatrix} = \begin{bmatrix} P_x^{sp} \\ P_y^{sp} \\ P_z^{sp} \end{bmatrix} + \begin{bmatrix} e_{11} & e_{12} & e_{13} & e_{14} & e_{15} & e_{16} \\ e_{21} & e_{22} & e_{23} & e_{24} & e_{25} & e_{26} \\ e_{31} & e_{32} & e_{33} & e_{34} & e_{35} & e_{36} \end{bmatrix} \begin{bmatrix} \epsilon_{xx} \\ \epsilon_{yy} \\ \epsilon_{zz} \\ \epsilon_{yz} \\ \epsilon_{xz} \\ \epsilon_{xy} \end{bmatrix}$$

Here P^{sp} denotes the spontaneous polarization vector, and the quantities e_{ij} denote the strain-charge piezoelectric coefficients.

The strain tensor ϵ can be obtained in one of various ways:

- ▶ By reading the strain tensor from the TDR file generated in Sentaurus Process or Sentaurus Interconnect through the **mechanics** command.
- ▶ The strain tensor ϵ is computed from the stress tensor σ by the generalized Hooke's law for anisotropic materials: $\epsilon = S\sigma$
- ▶ A constant strain tensor can be specified in the command file.

The new strain model for piezoelectric polarization complements the existing models in Sentaurus Device, such as the simplified model by Ambacher et al. [3,4] or the stress-based model using the piezoelectric coefficients d_{ij} .

Hot-Carrier Stress Degradation Model

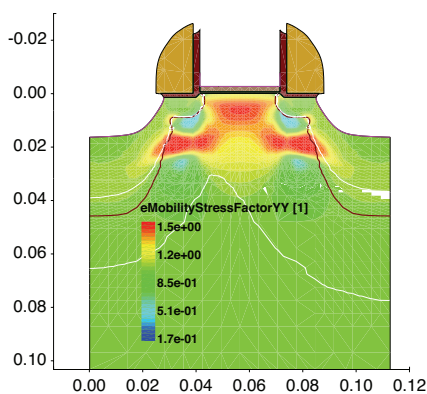
A new general degradation model suitable for modeling time-dependent trap generation in MOS-based devices has been implemented in Sentaurus Device. The hot-carrier stress (HCS) degradation model [5] includes different mechanisms that contribute to bond breakage and the formation of interface traps:

- ▶ Single-particle (SP) processes, where a single particle is responsible for bond breakage
- ▶ Multiple-particle (MP) processes, where the combined actions of several particles contribute to bond breakage
- ▶ Field-enhanced thermal (TH) processes, where thermal interactions with the lattice contribute to bond breakage

The model also includes a bond-dispersion option that accounts for bonds with a distribution of activation energies.

Reaction rates for the SP and MP processes in the HCS degradation model are dependent on the carrier distribution function that enters through scattering-rate integrals that include the full band structure density of states and group velocity. The carrier distribution function is obtained from the Spherical Harmonic Expansion (SHE) solution of the Boltzmann transport equation.

The new HCS degradation model was applied to a typical LDMOS device shown in Figure 9 (top).



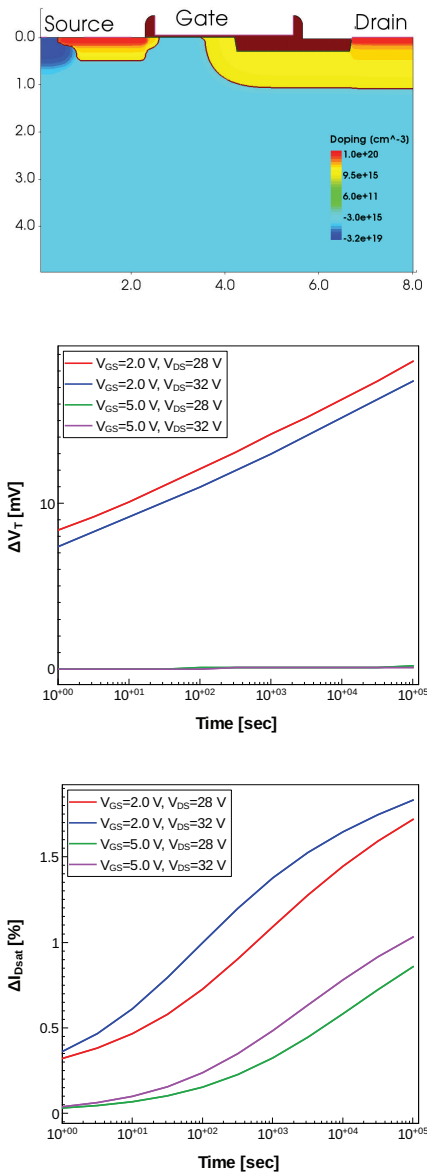


Figure 9: LDMOS device used in HCS simulation (top). Drift of threshold voltage (middle). Drift of saturation current (bottom) as a function of stress time for four different stress conditions.

Figures 9 (middle) and (bottom) show, respectively, the degradation in threshold voltage V_T and in saturation current $I_{D,sat}$ simulated with the HCS degradation model. When applied to different bias conditions and degradation times, the model exhibits typical behavior for such devices: for low gate bias we observe relatively large threshold voltage degradation but for high gate bias these changes are less significant.

Quantization and Mobility Modeling for III-V CMOS

Accurate modeling of the potential performance of devices with III-V channel materials requires accounting for the more complicated band structure of III-V's, including multiple valleys and strong band non-parabolicity, as well as geometrical quantization, which produce a dependence of the carrier transport on the layer thickness.

In the K-2015.06 version of Sentaurus Device, both modeling and calibration enhancements have been made with these considerations in mind to enable more accurate simulation of III-V CMOS devices. With regards to calibration, the Density Gradient quantum model and the bulk and inversion layer mobility models have been calibrated for relaxed InGaAs across the full range of mole fractions. With regards to mobility modeling, the Subband mobility correction models have been extended to account for the various bands of III-V materials, enabling the treatment of the stress and layer thickness dependence of the inversion mobility. (Parts of this work were supported by the European Community's Seventh Framework Program (FP7/2007-2013) under grant agreement 619326-III-V- MOS Project.)

Calibration of Density-Gradient and Low-Field Mobility for InGaAs

The latest parameters concerning the quantization effect and the inversion layer mobility for InAs, GaAs, and In_{1-x}Ga_xAs have been updated in MaterialDB folder of Sentaurus Device. The density gradient model is calibrated with respect to the 1D Schrödinger solver of Sentaurus Band Structure by fitting the factor gamma (γ) in the density gradient model using the inversion layer density values over a range of gate voltages as optimization target. Figure 10 shows the inversion layer density and the carrier distributions in a 10nm thick In_{0.53}Ga_{0.47}As double gate structure.

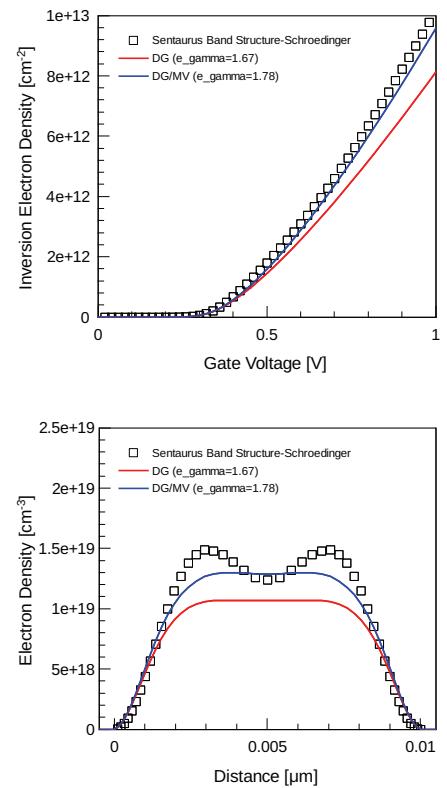


Figure 10: Inversion layer densities (top) and carrier distribution (bottom) at a gate voltage of 1V for a 10nm thick double-gate (110) MOS structure with In_{0.53}Ga_{0.47}As channel: red line is simulated with density gradient model and blue line is simulated with combination of multivalley and density gradient models; in both cases, e_{gamma} parameters have been optimized.

The MLDA model gives similar agreement for film thicknesses larger than 7nm and better results for film thicknesses smaller than 7nm. No calibration or parameter extraction is necessary for the MLDA model.

As for the low field mobility models, coefficients for ConstantMobility, DopingDependence, and for the Philips Unified Mobility Model (PhuMob) are extracted by empirical fitting based on reference literature. A first version of electron inversion layer mobility parameters has been calibrated for the Inversion and Accumulation Layer Mobility model (IALMob) with respect to the 1D mobility calculator of Sentaurus Band Structure and available experimental data. Figure 11 presents the curves of



mobility versus electric field for $\text{In}_{0.53}\text{Ga}_{0.47}\text{As}$ material when implementing the **IALMob** model and the interface charge density models with calibrated parameters.

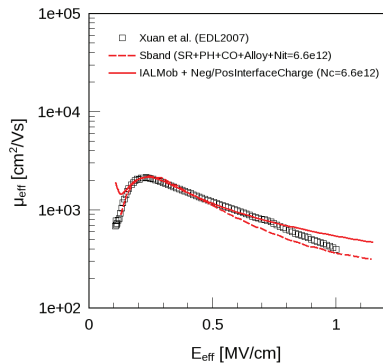


Figure 11: Effective electron mobility versus effective electric field for $\text{In}_{0.53}\text{Ga}_{0.47}\text{As}$ MOSFET with Al_2O_3 gate dielectric. Dot line: using 1D mobility calculator of Sentaurus Band Structure. Thick line: using IALMob and InterfaceCharge models with calibrated parameters. Squares: Experimental data from Ref [5].

Subband Mobility Correction Models for Layer Thickness Dependence

Geometrical quantization is usually strong in III-V materials because of the small electron effective mass in the Γ valley. Such quantization creates a band gap widening effect and changes the carrier mobility in thin III-V layers. Figure 12 shows the geometry and doping in the active area of III-V FET presented by Intel at the IEDM in 2009 [7]. The original thickness of 10nm for the $\text{In}_{0.7}\text{Ga}_{0.3}\text{As}$ channel is used.

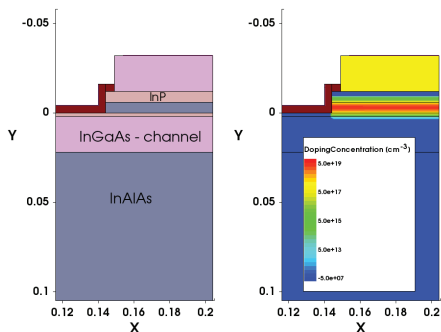


Figure 12: Geometry (left) and doping (right) of III-V FET with $\text{In}_{0.7}\text{Ga}_{0.3}\text{As}$ channel.

The multi-valley subband mobility correction models were enhanced to work with arbitrary bands of III-V materials. Together with the multi-valley MLDA model, these enhancements make it possible to account for the relative impact of geometrical confinement on the carrier transport masses, scattering rates, and ultimately in the carrier mobility in such III-V channels. Figure 13 shows simulation results of the III-V FET drain current in the linear regime for the channel thicknesses 7, 10, and 20nm. These results exhibit very strong geometrical confinement and layer thickness effects in such applications.

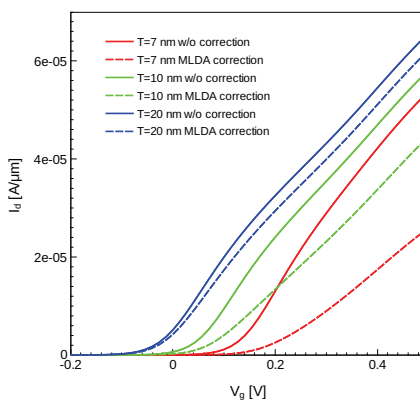


Figure 13: Simulated $I_d V_g$ curves of III-V FET in linear regime with and without Subband MLDA mobility correction for 7, 10, and 20nm channel thicknesses.

Improved Calibration for SiGe

Updated parameter files for Silicon, SiliconGermanium, and Germanium are available in the MaterialDB folder of Sentaurus Device for version K-2015.06. The files contain new parameters for the electron and hole inversion layer mobility, extending the calibration to very high channel doping concentration and covering the whole mole fraction range from 0 to 100% germanium. As a reference for calibration, the 1D mobility calculator of Sentaurus Band Structure is used. Comparison and validation with mobility measurements has been done where high quality experiments are available.

Sentaurus Device Monte Carlo

Screened Ionized Impurity Scattering

Sentaurus Device Monte Carlo (MC) K-2015.06 now supports screened ionized impurity scattering which is modeled using the Brooks-Herring approach where the screening length is computed under degenerate conditions.

By default, a doping-dependent prefactor of the rate for impurity scattering is calibrated to the Masetti mobility measurements [8]. In the case of electrons, the default calibration refers to arsenic doping. It is now also possible to switch this calibration off in order to study the importance of this calibration. Furthermore, for electrons there is now also a calibration for phosphorous doping.

The influence of these calibrations is illustrated by simulating n-type FinFETs as a function of the gate length. Figure 14 shows a FinFET with a gate length of 15nm, a fin width of 5.5nm and a fin height of 20nm. The doping level in the source/drain regions is $3 \times 10^{20} \text{ cm}^{-3}$, and in the extension regions $1.5 \times 10^{20} \text{ cm}^{-3}$, while the channel is undoped. The general features of the Monte Carlo approach employed are described in Ref. [9].

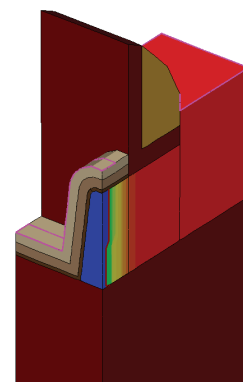


Figure 14: Geometry and doping profile of the FinFET using in MC simulations with the new screened ionized impurity scattering. Gate length $L=15\text{nm}$, fin height $H=20\text{nm}$, fin width $W=8.5\text{nm}$ at the top and a sidewall angle of 7° .

Figure 15 shows the drain current as a function of the gate length. It can be seen that the effect of the impurity scattering



calibration increases significantly at smaller gate lengths. The reason is that in shorter devices the relative contribution of source/drain and extension resistance to the total resistance becomes more important; therefore accurate modeling of ionized impurity scattering is crucial to predict short-channel device performance. Furthermore, ionized impurity scattering is now by default screened with the lattice temperature instead of with the carrier temperature.

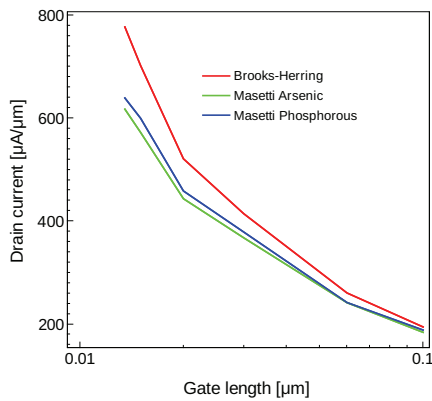


Figure 15: Drain current as a function of gate length for FinFETs like the one shown in figure 14 using the default Brooks-Herring mobility model (red curve) and using the Masetti mobility model calibrated for arsenic (green) and phosphorous (blue) doped silicon.

Subband and Inversion-Layer Mobility Calculator

Two major enhancements have been made to the subband and low-field mobility calculation features of Sentaurus Band Structure, namely the ability to solve the 8-band $k\cdot p$ Schrödinger equation and the addition of surface roughness scattering for mobility calculations for 2D FinFET and nanowire cross-sections.

Schrödinger Equation Solvers

In addition to the existing 2-band $k\cdot p$ and 6-band $k\cdot p$ Schrödinger solvers, a new 8-band $k\cdot p$ Schrödinger solver has been added. The 8-band model describes the lowest conduction band and the three highest valence bands around the Γ point,

and is particularly applicable to direct band-gap materials with zinc-blende crystal structure, such as InGaAs [10]. Strain effects, such as modifications to the band gap and dispersion, can be treated within the context of the 8-band $k\cdot p$ solver as well. As with the other Schrödinger solvers in Sentaurus Band Structure, the 8-band $k\cdot p$ solver can be applied to 1D or 2D device structures.

As an example, Figure 16 shows the electron and hole subband dispersion around the Γ point in the $\langle 100 \rangle$ direction for a relaxed, 10nm quantum well composed of $\text{In}_{0.53}\text{Ga}_{0.47}\text{As}$. Due to confinement, the resulting band gap is larger than the bulk band gap. The non-parabolicity of the electron subbands is the consequence of the coupling between conduction and valence bands.

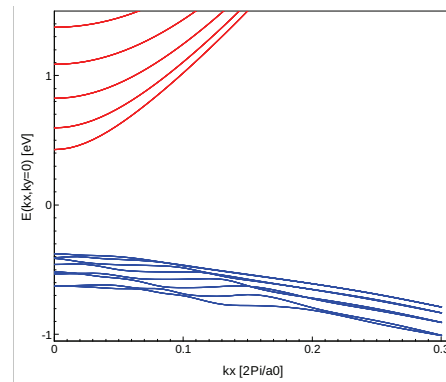


Figure 16: Confined band structure in $\langle 100 \rangle$ direction, computed with the new 8 band $k\cdot p$ Schrödinger solver for a 10nm quantum well composed of $\text{In}_{0.53}\text{Ga}_{0.47}\text{As}$.

Surface Roughness Scattering for 2D Structures

The Kubo-Greenwood formalism has been extended to include surface roughness scattering for the calculation of low-field mobility in 2D structures such as FinFET and nanowire cross-sections based on the subbands computed from the 2D Schrödinger solver. Either the parabolic or one of the $k\cdot p$ Schrödinger solvers (2 $k\cdot p$, 6 $k\cdot p$ or 8 $k\cdot p$) can be used. This new scattering model can treat cross-sections of arbitrary shape and allows the surface

roughness amplitude to be specified as a function of surface orientation.

Simulation of Spin-Transfer Torque Devices Using Sentaurus Device Spintronics

Almost half a century after the “golden age” of ferrite core memory, magnetic RAM is returning to the scene in the guise of spin-transfer torque (STT) RAM. However, the rules of the game have changed: The millimeter-sized magnetic rings of the old core memory have been superseded by stacks of thin films with thicknesses in the nanometer range and that are patterned by advanced photolithographic processes. The mechanisms for programming and read-out also have changed: Instead of setting the magnetization of the storage node using the magnetic field around currents flowing in wires, direct magnetization switching due to injection of spin-polarized currents is used in STT-RAM, and read-out of the storage state is based on the tunneling magnetoresistance (TMR). With SRAM-like speed, DRAM-like density, high endurance, and flash-like nonvolatility, this rejuvenated magnetic memory has many of the characteristics demanded of *universal memory* (see Figure 17 for the expected application space of STT-RAM).

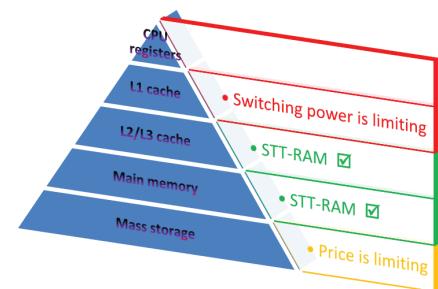


Figure 17: Application space for STT-RAM in the memory hierarchy of a computer system.



This calls for simulation support for a new class of devices that rely not only on the charge but also on the spin of the electrons, thereby evolving from traditional electronics into the realm of *spintronics*. The Sentaurus Device Spintronics option adds this functionality to the Sentaurus Device simulator.

The most basic building block of an STT device is the magnetic tunnel junction (MTJ). It consists of two ferromagnetic regions separated by a tunneling barrier. One of the ferromagnetic layers (the *pinned layer*) typically has its magnetization fixed during the manufacturing process, for example, by annealing inside a strong magnetic field. The magnetization of other ferromagnetic layer (the *free layer*) is intended to be modified during device operation. Interaction between the magnetic moment associated with the spin angular momentum of the conduction electrons and the magnetization of the ferromagnetic material splits the conduction band density-of-states into energetically favorable *majority spin* states and energetically unfavorable *minority spin* states (see Figure 18). The current passing through a ferromagnetic region readily becomes polarized according to the ratio between majority and minority spins density-of-states at the Fermi energy.

In a MTJ geometry, the magnetization inside each ferromagnetic region defines the majority and minority spin directions. When fixed voltage is applied across the MTJ, the resulting tunneling current is seen to depend on the relative orientation of the magnetization directions on either side of the junction: for parallel magnetization, the current is at a maximum; for antiparallel magnetization alignment, a current minimum is observed. This is called the *tunneling magnetoresistance* effect.

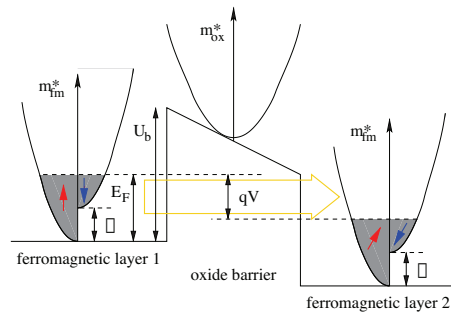


Figure 18: Schematic depiction of spin selective tunneling through an MTJ. Colored arrows denote the direction of majority spin (red arrows) and minority spin (blue arrows) on either side of the barrier.

Tunneling magnetoresistance can be used to detect the magnetization configuration of an MTJ. However, spin selective tunneling provides an additional mechanism for modifying the magnetization configuration. The tunneling current through the MTJ consists of spin-polarized electrons and, consequently, transports not only charge but also angular momentum. Upon arrival on the other side of the tunneling barrier, the tunneling electrons have their spin realigned parallel to the magnetization direction of the receiving layer. However, angular momentum is a conserved quantity and cannot simply vanish. Instead, the torque that aligns the spin of the tunneling electrons with the magnetization direction is accompanied by an equal and opposite torque that acts on the exchange-coupled inner-shell electrons and, therefore, rotates the magnetization direction. This is the eponymous *spin-transfer torque* of STT-RAM. Electrons tunneling from the fixed layer to the free layer favor parallel magnetization alignment; conversely, electrons tunneling from the free layer to the fixed layer favor an antiparallel configuration.

Magnetic anisotropy can be used to define a pair of stable states separated by an energy barrier (for example, parallel and antiparallel to the magnetization of the pinned layer). Anisotropic magnetic behavior may arise from the shape of the magnetic sample (a

compass needle has stable magnetization along its length; simple magnetic thin films prefer being magnetized in-plane), and the material may exhibit magnetocrystalline anisotropy (for example, $L1_0$ -ordered alloys such as PtFe with alternating planes of Pt and Fe atoms). In addition, there are interface effects: Interfaces between ferromagnetic and paramagnetic materials tend to favor magnetization normal to the interface—in very thin films, this may prevail over the shape anisotropy and give rise to perpendicular magnetic anisotropy even in the absence of magnetocrystalline anisotropy.

Well-defined stable states, a method for manipulating them, and a method for sensing them are the ingredients needed for memory operation. Figure 19 shows the time evolution of the magnetization inside the free layer of an in-plane MTJ during switching from the antiparallel (AP, high resistance) to the parallel (P, low resistance) state.

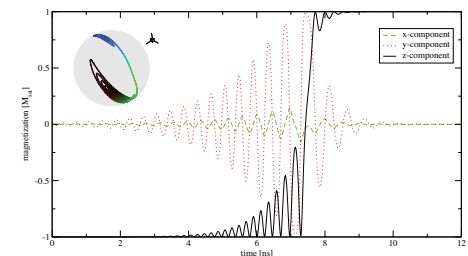


Figure 19: Time evolution of the magnetization direction during AP to P switching in an in-plane MTJ at constant voltage.

Of course, simulation is not limited to a single MTJ. More general structures like stacked MTJs with exchanged coupled free layers forming a synthetic antiferromagnet (SAF) also are supported. MTJs and conventional electronics devices such as access transistors may be present in the same structure. Figure 20 shows the circuit of an MTJ-assisted nonvolatile SRAM cell. Mixed-mode simulation results of this setup are depicted in Figure 21.

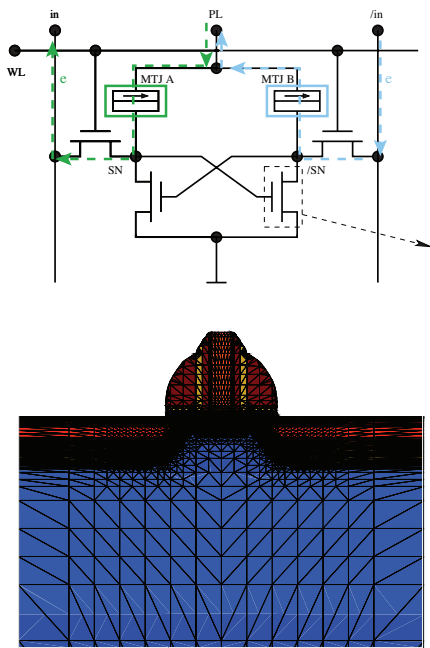


Figure 20: MTJ-assisted nonvolatile SRAM circuit.

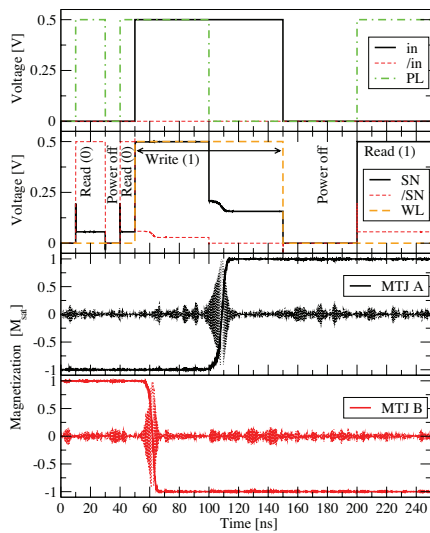


Figure 21: Mixed-mode simulation results for MTJ-assisted nonvolatile SRAM circuit.

Finally, beyond the use of MTJs in memory devices, there are also proposals for STT-based logic. Figure 22 shows a spin-torque majority gate: four terminals (three inputs MTJs, one output MTJ, and the pinned

layer magnetization points *up*) share the same cross-shaped free layer. In a majority gate, the value presented at the majority of the input ports will be propagated to the output. In the example shown, the free layer magnetization was initially pointing *up*. Two input ports (B, C) are trying to switch the magnetization; port A is opposing the switching, but is overwhelmed. Shortly after the magnetization snapshot in Figure 22 was taken, the *down* alignment of the magnetization has spread all the way to the output port.

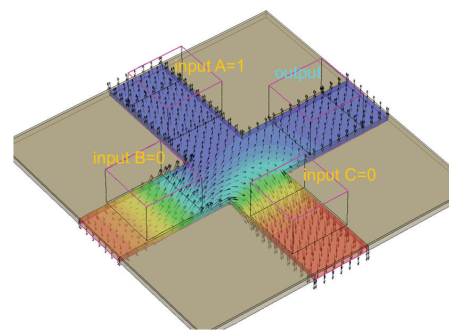


Figure 22: Magnetization distribution during switching of an STT-majority gate.

Sentaurus Device Optoelectronics

The K-2015.06 release of Electro-Magnetic Wave solver (EMW) in Sentaurus Device features enhancements in far-field computation and a real-time convergence monitor. Both of these enhancements address the simulation of CMOS image sensors and other photo detectors.

Far-field Computation

The backscattered fields from the pixels of CIS can inadvertently interact with the macro lens design. Considering the distance between the CIS pixels and the macro lens, and the visible wavelength scale of the fields, the backscattered fields can be treated as far field radiation. Metrics such as diffraction efficiency can be computed, and periodicity of the CIS array can be accounted for. EMW computes the far-field through a near-field to far-field transformation, that is,

by means of the equivalence theorem and a Green's function projection of the near field current source. The near-field is extracted in the scattered-field region at the end of an EMW simulation. The calculated far-field intensity is represented as a function of the polar diffraction angle, θ , and the azimuthal diffraction angle, φ , on a flattened polar grid, as illustrated in Figure 23.

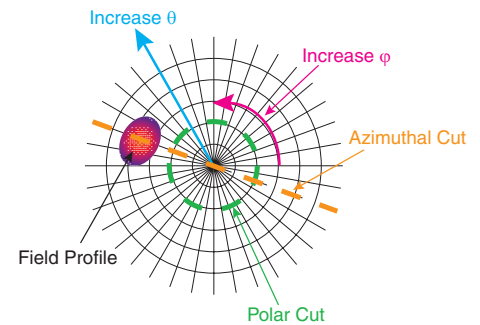


Figure 23: Illustration of polar plot for representation of far-field.

The far-field power is computed by integrating the far-field intensity over a user-supplied solid angle. Periodicity of the CIS array is assumed to be in the x and y directions, and the diffraction modes for a given array size are computed a priori assuming that the CIS array's periodicity is extended to infinity. For the computation of the far-field of a finite CIS array, the near-field resulting from the EMW simulation is replicated accordingly, after which the near-to-far field transformation is applied. With increasing periodic array size, the diffraction modes will converge to a delta value at their maxima, as illustrated in Figure 24. Note that integrating the diffraction mode within its modal cone of solid angle should yield the same result as the periodic array size is varied. The far-field computation is also available via post-processing if the near-field is saved in the preceding EMW simulation.

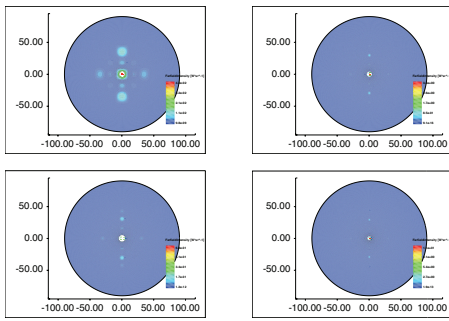


Figure 24: Far field Intensity for (top left) single CMOS image sensor pixel, (top right) 2x2 pixel array, (bottom left) 3x3 pixel array, (bottom right) 4x4 pixel array.

EMW Convergence Monitor

FDTD simulations are usually long running, so it is useful to have a real-time monitor to track the state of convergence. Such information allows the user to intervene in a simulation that might not be converging well. The maximum deviation of the entire detector domain is continuously saved into a file that can be plotted in real-time in Sentaurus Visual, an example of which is illustrated in Figure 25. In addition, the EMW simulation can be terminated at any time, and the vectorial field results at that instance of termination will be saved for later processing.

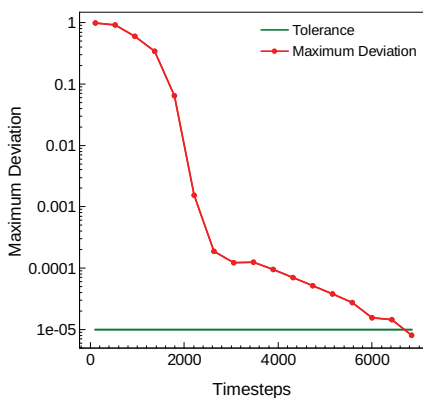


Figure 25: Maximum deviation versus time steps during an EMW simulation (red curve). The green line denotes EMW tolerance setting of 10^{-5} .

Usability Improvements

The K-2015.06 release of TCAD Sentaurus contains a number of features designed to improve user productivity. It is now much easier to generate implant tables on the fly and to define doping in arbitrarily shaped regions. When debugging difficult convergence problems, user can now conveniently check if switching to a slow transient would help convergence without having to re-write section of the Sentaurus Device input file. Users can also now write generic input files that do not depend on the exact spelling of the contact names and work with devices with a large number of contacts without the need to declare each of them individually. When working in mixed-mode simulations, it is no longer necessary to re-write standard HSPICE netlists in Sentaurus Device syntax.

Several features are added to help analyze converge and mesh quality, and a new visualization utility is now available to permit users to quickly find information in the tool log files.

Transient Ramp: an Alternative Quasistationary-like Syntax for Transient Simulation

For certain applications, simulation convergence may improve if a slow transient ramp is applied instead of a quasi-stationary ramp. Examples include wide-bandgap semiconductors, devices with trap states, and, sometimes, breakdown simulations. To improve usability, Sentaurus Device K-2015.06 now allows switching from a quasi-stationary to a (slow) transient simulation with minimal user effort, for example by simply replacing the `Quasistationary` keyword with the `Transient` keyword. It is no longer necessary to make considerable changes in the Sentaurus Device input file for such a switch.

Regular Expression Matching for Electrodes and Thermodes

In device structures containing many contacts, it is now possible to define the contact boundary conditions with a single command. For example, a group of contacts may be defined as ground with a single command, while another single command sets the bias for another group. Users may also want to define a Sentaurus Device input file with case insensitive naming for the same contact (such as "gate" "Gate", and "GATE"). This can be done with Perl-like regular expressions for pattern matching in the `Electrode`, `Thermode`, and `Solve/Goal` sections. This feature removes the restriction that electrodes and thermodes be defined by a unique string identifier.

HSPICE Netlists

Sentaurus Device supports a number of HSPICE compact transistor models, such as the level 72 BSIM-CMG model for multi-gate MOSFET devices, or the level 73 HiSIM_HV model for high voltage applications. These and other compact models can be used in mixed-mode simulations in Sentaurus Device.

Sentaurus Device K-2015.06 can now read standard HSPICE netlist files directly by loading them in the `system` section. A more relevant subset of the HSPICE language is recognized, including:

- ▶ HSPICE parameters (`.PARAM` statement)
- ▶ Sub-circuits with subcircuit arguments
- ▶ Arithmetic expressions

Design engineers can now work with standard SPICE netlist descriptions without having to re-write the netlist in the Sentaurus Device syntax.

Sentaurus Device also offers an extension of the HSPICE syntax so that even physical devices can be specified directly in the HSPICE netlist. First, a physical device must be defined in terms of its contact names:

```
.SDEVICE igbt gate emitter
collector
```

Afterwards this physical device can be added to the circuit like any other compact model:

```
x1 g e c igbt
```

Effective Mobility Current Plot PMI Enhancements

The `EffectiveMobility` current plot Physical Model Interface (PMI) has been made more versatile with the addition of several new features:

- ▶ The `EffectiveMobility` PMI can be included multiple times in the same `CurrentPlot` section, making it possible to perform several different extractions in the same command file
- ▶ Carrier density computed with Spherical Harmonic Expansion (SHE) can be used as a weighting function for the quantities being extracted
- ▶ The extractions can be performed over an extended portion of the channel as an alternative to extraction at a single point. Two methods for accomplishing this are provided: (1) an interface-area weighted average of line integrals that span the channel, and (2) a volume-based average over the channel region.
- ▶ The list of extracted quantities has been expanded and includes average field and average carrier densities (in addition to effective fields and sheet densities) and effective stress factors for mobility.

Sentaurus Device Enhancements for Convergence Monitoring

Automatic Activation of Convergence Quality Monitoring

The `CNormPrint` option of the `Math` sections in Sentaurus Device allows printing, for each iteration, of the maximum error encountered in the device per solved equation. Similarly, the `File` section option `NewtonPlot` can be used to identify where in the device, and for which equations, large errors occur. This information can be helpful for making adjustments to simulations with poor convergence.

In this release, `CNormPrint` and `NewtonPlot` are activated automatically when Sentaurus Device is on the verge of failing due to convergence issues. This makes the information provided by

`CNormPrint` and `NewtonPlot` immediately available for analysis, removing the need to rerun the failed simulation with the options switched on in order to obtain this information.

Simulation Statistics for Plotting and Output

Sentaurus Device now provides an option to output simulation statistics to the current plot file so it can be visualized in Sentaurus Visual or Inspect. The statistics include the right-hand side (RHS) error, iterations, step size, number of restarts, simulation times, and cumulative statistics. All statistics are recorded at each bias or time point. This capability provides insight into the overall behavior of a simulation, enabling users to create optimal solution strategies.

In addition, an option has been provided to write the cumulative statistics for the full simulation to design-of-experiments (DOE) variables in the Sentaurus Device output file. These DOE variables can be extracted and utilized within Sentaurus Workbench.

Saving and Viewing of Mesh Quality Information

When Sentaurus Device reads in a device structure, the `BoxMethod` utility computes the control volumes associated with each vertex in the mesh. This utility also computes information related to mesh quality. In release K-2015.06 users can now save this mesh quality information to the Sentaurus Device structure output file. Part of this mesh quality information is associated with a mesh vertex, and part with a mesh element. For example, the output for the mesh information can be activated with:

```
Plot {
  BM_ElementsPerVertex
  # location = vertex
  BM_IntersectionNonDelaunay
  Elements # location = element
  . . .
}
```

As an example Figure 26 shows, for a simple 2D mesh, the data field which contains the number of vertices per element and

Figure 27 shows the intersection parameters for non-Delauney elements. It can be seen that all obtuse triangles show a non-zero intersection parameter.

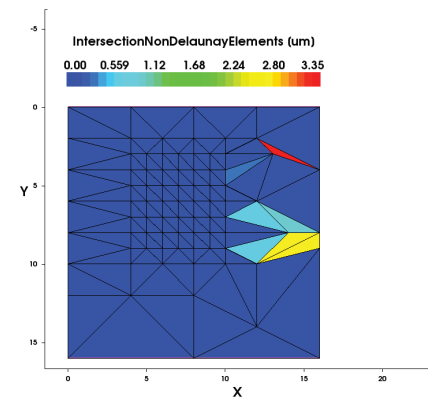


Figure 26: Visualization of the number of vertices per element for a simple 2D mesh.

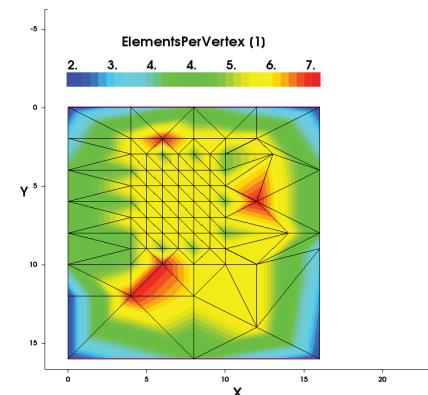


Figure 27: Visualization of the intersection parameters for non-Delauney elements for a simple 2D mesh.

Log file Browser

TCAD tool log files contain a wealth of useful information. However, it is sometimes difficult to find the relevant information in this unstructured text file. This challenge is addressed, at least partially, with the new log file browser. When Sentaurus Process, Sentaurus Interconnect and Sentaurus Device are invoked with the command line option `--xml`, the log file content is annotated with XML-like tags, thus enabling the log file browser to access the information in a structured manner. For example, users



navigate the tree-like hierarchy of the tags to find a particular section of interest. It is also possible to visualize only sections with a certain tag within the selected hierarchy. The log file browser can be launched from the Sentaurus Workbench Node Explorer dialog box by double-clicking on the file with the extension `.xml`. This utility runs within the default web browser. Figure 28 shows a Sentaurus Process log file displayed in the log file browser. For Sentaurus Process and Sentaurus Interconnect, custom tags added to the process flow, for example, tags for specific user-defined process modules, will be added to the set of automatically generated tags to further structure the log file output.

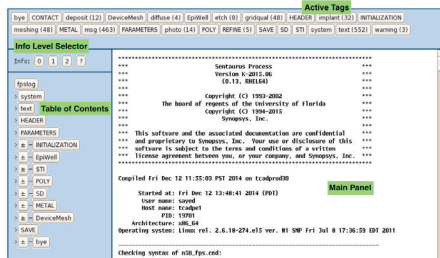


Figure 28: The log file browser allows accessing the wealth of information in the log files in a structured manner and supports interactive selection and as well as filtering.

Sentaurus Visual

Sentaurus Visual is a visualization tool that allows the user to interactively analyze and explore data obtained from simulations. In Sentaurus Visual K-2015.06, the following new features have been implemented in order to improve the functionality of the software.

Value Blanking

Several changes have been made to enhance the way blanking is made. Now it is possible to apply a blanking filter not only to 3D, but also to 2D plots. In addition, it is now possible to assign a logical operator to each blanking filter. In the past the constraints of each filter were only combined with a union operator. Now either union or intersection

operators can be assigned between filters which makes it possible to blank new kinds of areas (see Figure 29).

Another improvement was made regarding linked frames. Sentaurus Visual now applies value blanking operations consistently to linked plots.

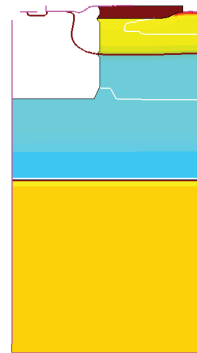


Figure 29: Value blanking for 2D plot. The constraints applied could not be performed without the intersection operator. Constrains used are $(x < -5) \cap (y < 5)$

Shifting and Scaling Curves

It is now possible to apply a shift and a scale value to a curve independently. This capability makes it possible to compare, in the same window, curves with different proportions or coordinates. The shifting and scaling can be applied to the x- and y-axes.

Iso-Surface Display

Another new feature is the option to visualize isosurfaces and isolines. This new functionality generates geometries that overlay the plot from where the data was taken. Each new geometry is an isosurface structure (or an isoline in two dimensions), with a set of regions and fields.

The new geometry has the same properties as a normal geometry, and the bulk and line colors can be changed like a regular region. The default bulk color of these structures is gray, but users can set a constant color for the entire new geometry (iso-geometry) in the creation dialog (see Figure 30).

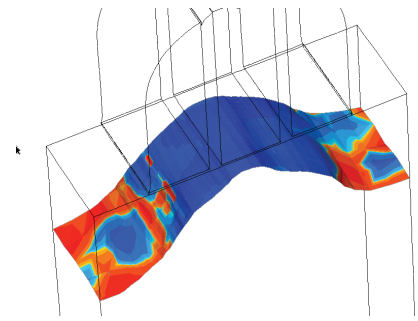


Figure 30: Example of iso-surface visualization: Doping profile on the iso-surface with the electrostatic potential of 0V

Option to Automatically Replace Old Curves with New Curves in Outline Plots

A new **Selection** panel has been implemented exclusively for outline plots. The curves displayed depend only on the datasets and variables selected in the panel. After the selection has changed, curves are created and removed according to the selection. This makes it very convenient to check through many outline curves.

The new **Selection** panel for cutlines has fewer buttons. The buttons to assign variables to the x-axis and the y-axis have been removed. The Selection panel maintains the **New Variable** button, and the new **Duplicate Plot** button is used to duplicate the current plot and to convert it into a non-cutline plot.

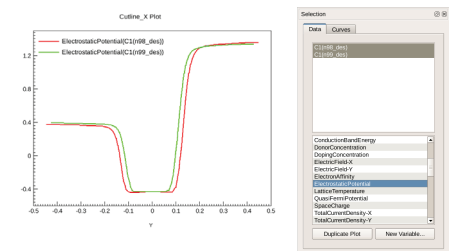


Figure 31: New selection panel for cutlines plots.

Display the Number of Mesh Points per Region

Two new enhancements were added to Sentaurus Visual to provide a direct way

to obtain information about the mesh and plot data. For 2D and 3D plots, the total number of points and elements of the dataset selected will always be displayed at the bottom of the window. For detailed information about the mesh point, a new dialog was added where the user can get the data needed. In the new dialog, the user can check the number of points and elements in a certain region, material or a group of regions and materials.

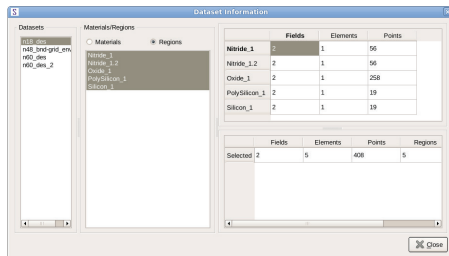


Figure 32: Dataset information dialog with mesh information data.

Duplicate XY plot

Sentaurus Visual can now duplicate XY plots. This can be used to compare datasets with similar properties or to easily replicate visualization characteristics in a new plot.

The properties replicated in the new plot are fonts, title, axes, ticks, scale, and curves.

To access to this new enhancement a new button was added to the Data panel and new parameters were added to `create_plot` command.

Sentaurus Workbench

Managing Experiments in Scenarios

Sentaurus Workbench K-2015.06 includes several usability enhancements to improve the support of scenarios.

Users can now add a new scenario and immediately define which experiments to include in the new scenario by specifying a node expression in the **Add Scenario** dialog box. As the result, a new scenario with the given name and experiments matching the given expression will be created.

In the new **Manage Membership in Scenarios** dialog box users can easily include or exclude selected experiments with or from multiple scenarios. The **Common Scenarios** field of the dialog lists the scenarios to be included in selected experiments. Any scenario added to this field will include all the selected experiments. Sentaurus Workbench excludes the selected experiments from all other scenarios that are not listed in the **Common Scenarios** field. In this dialog box, users can also create a new scenario that, being added to the **Common Scenarios** field, includes the selected experiments.

The **Remove Scenarios** dialog box removes scenarios from the project. In this case, Sentaurus Workbench first excludes the experiments from those scenarios. These experiments are not deleted from the project unless users explicitly select the **Delete Included Experiments From Project** option. By default this option is not selected, but it can be changed in the preferences.

Selected experiments can be deleted entirely from the project by selecting **Delete Experiments**. Otherwise selected experiments can be excluded from the current scenario by selecting **Exclude Experiments**, or pressing the **Delete** key, which keeps selected experiments in the project. The default scenario all contains **all** the experiments. However, when experiments are excluded from the scenario **all**, these experiments are removed from the project.

Flexible Creation of Parameters with Variation

Sentaurus Workbench K-2015.06 simplifies project setup by merging two separate dialog boxes **Add Parameter** and **Add Values** into one new dialog box **Add Parameter/Values**. The new dialog allows users to create a new parameter and specify its value and its placement in the flow. It also can be used to add values to existing parameters (see table below).

The Add Parameter/Values dialog box offers four modes of specifying values:

Users can sort the values in ascending or descending order, or keep the values unsorted. Three predefined formats are available to apply to the values (scientific, engineering, and integer). Finally, the values are displayed in the preview pane on the right side of the dialog box. All the defaults can be configured in the preferences.

By clicking **OK** or **Apply**, Sentaurus Workbench inserts the parameter with its values into the project flow. If the parameter exists, new values are added to the parameter. The new values appear in the project flow as they are displayed in the preview pane.

How to Partition User Run Limits Quota through Projects

Sentaurus Workbench has capabilities to support the efficient allocation of computational resources on computer networks. Run limits defined on a centralized level (global or site) or on user levels specify

Mode	What to do
List	Type the specific values using the user-defined list mode. Parameter values can be any alphanumeric value. In addition, values can include + (plus), - (dash), * (start), _ (underscore), . (dot), and : (colon). Space is prohibited; use it to separate values in the list.
Lin	Generate values using a linear scaling. Three of four parameters must be specified: the minimal value, the maximal value, the number of values to generate, and the step between values. The fourth parameter is calculated automatically. The value can be adjusted by changing any of these parameters.
Log	The same as Lin mode, but logarithmic scale is used.
Gaussian	Generates normally distributed values using a Gaussian scaling. Four parameters must be specified: the median, the standard deviation, the number of values to generate, and delta value to fix the range of generated values around the median.



a user quota. Previous versions of Sentaurus Workbench do not control how the user quota is distributed among projects. If several projects are launched simultaneously, the user quota may be reached in a single project run, while other running projects must wait until a free slot becomes available. Sentaurus Workbench K-2015.06 overcomes this limitation by introducing project run limits, allowing users to partition their user quota among different projects intended to run simultaneously.

When launching a project, users specify project run limits directly in the **Run Project** dialog box for each tool in the project. A value of 0 sets project run limits for the given tool. The number of simultaneously running instances of the tool in the current project is restricted exclusively by the user quota. A positive integer value applies a project run limit to the given tool: the number of concurrently running instances of the tool in the current project will be limited to the given number.

Project run limits affect only a given project and can be different among projects. Using reasonable project run limits, users can control how their run limits quota is distributed among projects, with low-priority projects assigned smaller numbers than high-priority projects. The minimum value is 1. The maximum number corresponds to the user quota.

By default, project run limits are switched off. Project run limits can be switched on or off at any time for an already running project, and are stored in the project. When a project is launched, the previous run limits are loaded into the **Run Project** dialog box, allowing the user to keep them or modify them.

Support of Individual Sentaurus Device Parameter Files

Sentaurus Workbench K-2015.06 now allows users to decide whether to use a standard or instance-specific parameter file. This

decision can be different for each Sentaurus Device instance in the project. The selection is made in the **Tool Properties** dialog box. By default, a new Sentaurus Device instance uses the common parameter file. Changing the default is possible in the tool database.

References

- [1] M. Moslehi and K. Saraswat, "Thermal Nitridation of Si and SiO₂ for VLSI", *IEEE Transactions on Electron Devices*, vol. 32, no.2, pp. 106-123, 1985.
- [2] B. Sklenard et al, "Atomistic investigation of the impact of stress during solid phase epitaxial regrowth", *physica status solidi c*, 11 (1), 97-100, 2014.
- [3] O. Ambacher et al, "Two dimensional electron gases induced by spontaneous and piezoelectric polarization in undoped and doped AlGa_N/Ga_N heterostructures", *Journal of Applied Physics*, 87(1), 334-344, 2000.
- [4] O. Ambacher et al, "Two-dimensional electron gases induced by spontaneous and piezoelectric polarization charges in N- and Ga-face AlGa_N/Ga_N heterostructures", *Journal of Applied Physics*, 85(6), 3222-3233, 1999.
- [5] S. Reggiani et al, "TCAD Simulation of Hot-Carrier and Thermal Degradation in STI-LDMOS Transistors," *IEEE Transactions on Electron Devices*, vol. 60, no. 2, pp. 691-698, 2013.
- [6] Y. Xuan et al, "Submicrometer inversion-type enhancement-mode InGaAs MOSFET with atomic-layer-deposited Al₂O₃ as gate dielectric," *IEEE Electron Device Letters*, vol. 28, pp. 935, 2007.
- [7] M. Radosavljevic et al, "Advanced High-K Gate Dielectric for High-Performance Short-Channel In_{0.7}Ga_{0.3}As Quantum Well Field Effect Transistors on Silicon Substrate for Low Power Logic Applications", in IEDM Technical Digest, Baltimore, USA, pp. 319-322, December 2009.
- [8] G. Masetti et al, "Modeling of Carrier Mobility Against Carrier Concentration in Arsenic-, Phosphorous- and Boron-Doped Silicon," *IEEE Trans. Electron Devices*, vol. 30, pp 764-769, 1983.
- [9] F.M. Bufler and L. Smith, "3D Monte Carlo Simulation of FinFET and FDSOI Devices with Accurate Quantum Correction," *J. Comput. Electron.*, vol. 12, pp 651-657, 2013.
- [10] T.B. Bahder "Eight band k-p model of strained zinc-blende crystals", *Phys. Rev. B* 41, 11992, 1990.